Applied Surface Science 601 (2022) 154144

Contents lists available at ScienceDirect

Applied Surface Science

journal homepage: www.elsevier.com/locate/apsusc

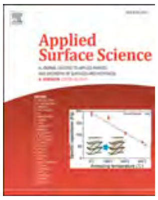

Full Length Article

Light-driven photothermal catalysis for degradation of toluene on CuO/TiO_2 Composite: Dominating photocatalysis and auxiliary thermalcatalysis

Caixia Liang [a,b], Caiting Li [a,b,*], Youcai Zhu [a,b], Xueyu Du [a,b], Yifu Zeng [c], Yihui Zhou [c], Jungang Zhao [a,b], Shanhong Li [a,b], Xuan Liu [a,b], Qi Yu [a,b], Yunbo Zhai [a,b]

[a] College of Environmental Science and Engineering, Hunan University, Changsha 410082, PR China
[b] Key Laboratory of Environmental Biology and Pollution Control (Hunan University), Ministry of Education, Changsha 410082, PR China
[c] Aerospace Kaitian Environmental Technology Co., Ltd, Changsha 410100, PR China

ARTICLE INFO

Keywords:
Toluene
CuO/TiO_2
Light-driven photothermal
Mechanism

ABSTRACT

Toluene, one of the main precures of photochemical smog and ozone pollution, is harmful to environment and human beings and has been attracted much attention. Herein, the CuO/TiO_2 composites with larger particle size synthesized by the wet precipitation method showed better performance than those synthesized by the sol–gel method for toluene removal. The CuO/TiO_2 composite (Cu/Ti = 1) exhibited the highest performance and excellent durability, attributing to their higher absorption of light and lower recombination of photogenerated charges. Electron paramagnetic resonance spectra confirmed that O_2^- radicals generated by surface adsorbed oxygen trapping electrons played a major role in photocatalysis. Under ultraviolet–visible light, the light-driven heat significantly increased the removal efficiency from 60% to 80%, and after adding infrared light, the removal efficiency further increased to 90%. Therefore, the photocatalytic effect played a dominant part in light-driven photothermal catalysis, and the photocatalytic performance and stability were greatly improved by reducing carbon deposition with light-driven heat. Furthermore, the mechanism of toluene degradation was studied by in situ diffuse reflectance infrared fourier transform spectroscopy.

1. Introduction

Toluene, the typical volatile organic compounds (VOCs), has aroused widespread concern as one of the main precursors of photochemical smog and ozone pollution [1]. It is reported that toluene emitted from various industries is harmful to humans owing to their toxicity, mutagenicity, and carcinogenicity [2–4]. Many technologies have been developed for effective control of toluene emission, such as adsorption [5], catalytic oxidation [6,7], and photocatalytic oxidation [8,9]. Among them, photocatalytic technology is considered to be promising for toluene removal due to its low-energy, and harmlessness [10]. However, the application of photocatalytic technology is limited by the insufficient utilization of light and the low stability [8,11]. Therefore, light-driven photothermal catalysis has been developed without external thermal energy input, which relies on the catalysts with strong absorption abilities of light and light-heat conversion [12,13]. Many black metal oxides (MnO_x, Co_3O_4) have been extensively used in light-driven photothermal catalysis [14–16]. Jia's group prepared different perovskites ($LaMnO_3$ and $LaTi_{1-X}Mn_XO_3$) with broad light wavelength absorption showing excellent performance [17,18]. Co_3O_4/TiO_2 nanocomposites with strong light absorption exhibited effective catalytic activity for benzene removal attributing to the synergetic effect between light-driven thermo-catalysis on Co_3O_4 and UV photocatalysis on TiO_2 [14].

TiO_2 is vigorously applied to photocatalytic technology owning to its excellent stability, low cost, and non-toxicity. Nonetheless, the development of TiO_2 is hindered by the wide band gap (3.20 eV) and poor utilization of visible light [19]. In this regard, many strategies have been applied to photocatalytic technology, including doping with metals [20,21], doping with non-metals [22,23], and compounding with other semiconductors [8,24]. The semiconductor composites have received much attention, which could facilitate the separation of electrons (e^-) and holes (h^+) owing to the formation of internal electric fields with different band gaps [25,26]. Furthermore, the interaction between complexes broadens the range of spectral absorption [27]. Copper oxide (CuO) is a typical p-type semiconductor with a narrow band gap

---

* Corresponding author at: College of Environmental Science and Engineering, Hunan University, Changsha 410082, PR China.
E-mail address: ctli@hnu.edu.cn (C. Li).

https://doi.org/10.1016/j.apsusc.2022.154144
Received 20 February 2022; Received in revised form 17 June 2022; Accepted 30 June 2022

(1.21–1.70 eV), which has been widely applied in various fields including NO_2 detection [28], CO_2 reduction [29], and VOCs degradation [30]. It is crucial that CuO exhibits a preeminent efficiency for VOCs degradation not only under light, but also under thermal treatment [31,32]. Zhang's group successfully established an interface between CuO and TiO_2 using a reduction-deposition method, which highly inhibited the recombination of the photogenerated holes and electrons [33]. Chen *et al.* [34] demonstrated that TiO_2 grown with CuO nanoclusters had high catalytic activity for formaldehyde removal under visible light. The CuO_X tremendously inhibited the recombination of e^- and h^+ through the transformation of the valence states of Cu. Zhou *et al.* [35] found the coexistence of Ti^{3+}, Ti^{4+}, Cu^{2+}, and Cu^+ promoted the separation of electrons and holes. And the band gap of CuO-TiO_2 was shortened obviously compared with pure TiO_2, indicating that the absorption greatly increased under visible light. Although CuO/TiO_2 composites are used for photocatalysis, few studies have investigated the process and mechanism for light-driven photothermal catalytic degradation of toluene. Moreover, few studies have investigated their performances in toluene removal, and the sperate contributions of photocatalysis and thermocatalysis in this process remain a puzzle.

In this work, composites of CuO and TiO_2 were successfully prepared by a simple wet precipitation method and the sol–gel method as an ideal light absorber, which can efficiently absorb light and trigger/accelerate catalytic reactions. The composites obtained by the wet precipitation method can greatly enhance the light absorption capacity, thus allowing more solar energy to be fully utilized and exhibiting excellent performance. To study the synergetic effects of light and heat, degradation performances of toluene were investigated under various conditions, including ultraviolet–visible (UV–Vis) irradiation, ultraviolet–visible-infrared (UV–Vis-IR) irradiation, room temperature, and heating mode, respectively. The catalytic activity and stability of the dark composite for toluene removal were evaluated under Xe lamp irradiation, and the effects of operating conditions on degradation were also discussed in detail. Moreover, the mechanism was analyzed by in situ diffuse reflectance infrared fourier transform spectroscopy (*in-situ* DRIFTs).

2. Experiment

2.1. Materials

Tetrabutyl titanate ($C_{16}H_{36}O_4Ti$, 98%), 2,4-pentanedione ($C_5H_8O_2$, A.R.), copper(II) nitrate trihydrate ($Cu(NO_3)_2·3H_2O$, A.R.), nitric acid (HNO_3, 68%) and ethanol were purchased from Sinopharm Chemical Reagents Co.,Ltd. All chemicals were used without further purification.

2.2. Catalysts preparation

Wet Precipitation Method: initially, a predetermined amount of $Cu(NO_3)_2·3H_2O$ was dissolved into 20 mL deionized water, and then solution was stirred at 80 ℃ for 1 h. After that, 10 mL $C_{16}H_{36}O_4Ti$ was typically added to the solution dropwise with intensively stirring at 80 ℃. Thereafter the suspension was reacted at 80 ℃ for about 4.5 h, then dried at 100 ℃ overnight. Conclusively, these samples were ground into powder and then heat-treated at 500 ℃ for 3 h under air atmosphere. Samples with different Cu/Ti molar ratios were denoted as follows: TiO_2(P) (Cu/Ti = 0), 1Cu2Ti(P) (Cu/Ti = 0.50), 2Cu2Ti(P) (Cu/Ti = 1).

Sol-gel Method: a predetermined amount of $Cu(NO_3)_2·3H_2O$, 0.50 mL 68% HNO_3 and 3 mL deionized water were dissolved in 16.80 mL absolute ethanol, and the obtained solution was slowly added to a mixed solution of 10 mL $C_{16}H_{36}O_4Ti$, 0.50 mL acetylacetone, and 20 mL absolute ethanol with intensively stirring at 20 ℃. The yellow solution was stirred vigorously at 20 ℃ until the gel formed. Then the gel was ageing for more than 12 h at 30 ℃, and dried at 60 ℃ for 12 h and 100 ℃ for 12 h. The obtained solid was heat-treated at 500 ℃ for 3 h under air atmosphere. Samples with different Cu/Ti molar ratios were denoted as follows: TiO_2(S) (Cu/Ti = 0), 1Cu2Ti(S) (Cu/Ti = 0.50), 2Cu2Ti(S) (Cu/Ti = 1).

2.3. Characterization

The structure and morphology of prepared samples were obtained by the scanning electron microscopy (SEM, Zeiss Sigma 300, German) and the transmission electron microscope (TEM, Titan G260-300, America). The X-ray diffraction (XRD) measurements were collected on a diffractometer in the range of 2θ from 10° to 80°. The N_2 adsorption–desorption isotherms were obtained from automatic specific surface area analyzer (Micromeritics APSP 2460, America), and the samples were degassed at 300 ℃ for 3 h before measurement under dynamic vacuum conditions. The specific surface area was calculated using Brunauer-Emmett-Teller (BET) method, and pore size was calculated based on Barrett-Joyner-Halenda (BJH) method. The valence states of chemical elements were analyzed by X-ray photoelectron spectroscopy (XPS, Thermo Scientific K-Alpha, America), equipped with a monochromatic Al Kα source. The optical absorption properties of the samples were carried out by UV–Visible diffuse reflectance spectra (UV–Vis DRS, Lambda750 PE, America). The surface functional groups of catalyst were tested by Fourier Transform infrared spectroscopy (FTIR, Thermo Scientific Nicolet iS20, America). The transient photocurrent responses and Mott-Schottky plots were measured by an electrochemical workstation with three-electrode system (CHI760E, China) in 0.50 M Na_2SO_4 solution. The samples were dispersed in a solution of naphthol (5%), and the suspension obtained after 4 h of sonication was uniformly coated on conductive glass (FTO). Then, the working electrodes were obtained by drying the conductive glass at 50 ℃. The transient photocurrent was measured under Xe lamp irradiation with a wavelength range of 320–780 nm and an illumination intensity of 400 mW/cm^2, alternating on and off light every 20 s. The initial voltage is the open circuit voltage. The electron paramagnetic resonance (EPR) spectra were characterized by Bruker EMXPLUS (Switzerland) with 5,5-dimethyl-1-pyrroline N-oxide (DMPO) as a radical scavenger at room temperature. In situ DRIFTs experiments were carried out by a Nicolet iS50 FT-IR spectrometer (America) equipped with an in situ diffuse-reflectance cell and a reaction chamber.

2.4. Experiment for toluene removal

The catalytic oxidation of toluene was carried out in a continuous system, as shown in Fig. 1. The experiments were irradiated by a 300 W Xe lamp (PLS-SXE300 +). For each experiment, 0.40 g catalyst was uniformly tiled on the sand core with a diameter of 80 mm. The toluene gas (500 ppm) was obtained by flowing nitrogen with ice-water bath, and the simulated air flow rate was 50 mL/min (20 vol% O_2, 0–2.0 vol% H_2O, N_2 as the balance gas). The simulated gas flow rate was controlled by the mass flow controller (MFC). After exposure to flow gas for 1 h to reach adsorption saturation, turn on the Xe lamp to activate the catalysts. The treated toluene was analyzed online by a gas chromatograph (GC, GC-2014C, SHIMADZU) equipped with a flame ionization detector (FID). The removal efficiency of toluene and CO_2 yield were calculated via the following equation:

$$\eta\ (\%) = \frac{C_{in} - C_{out}}{C_{in}} \times 100\% \quad (1)$$

$$CO_2\ yield\ (\%) = \frac{C_{CO_2}}{7*(C_{in} - C_{out})} \times 100\% \quad (2)$$

where η is the removal efficiency of toluene, %, and C_{in} and C_{out} are the concentrations of toluene at reactor inlet and outlet detected by the GC, ppm, and C_{CO2} is the concentrations of CO_2 at reactor outlet detected by PGA-650 (Phymetrix, America), ppm.

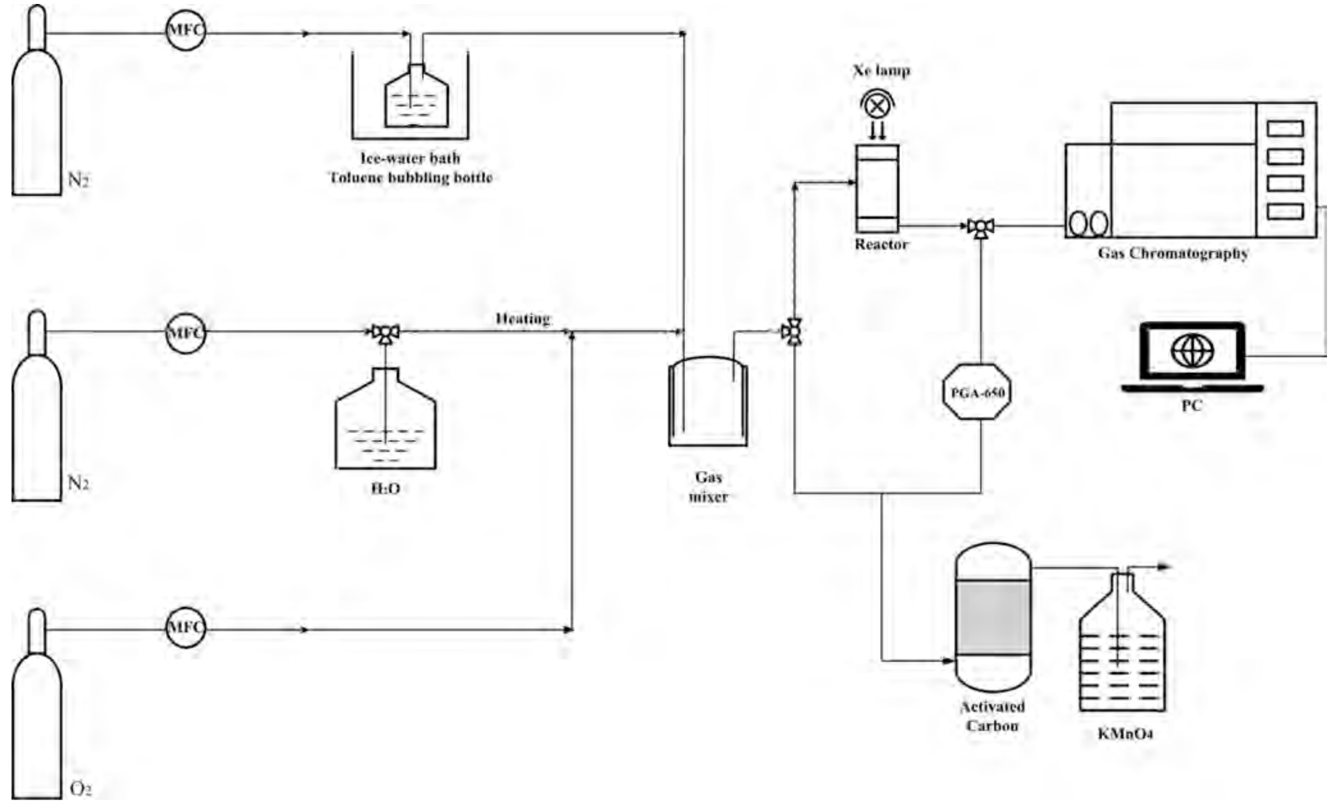

Fig. 1. Catalytic system for toluene removal.

3. Results and discussion

3.1. Catalytic performance

The catalytic performance of as-prepared catalysts was investigated under UV–Vis irradiation for 120 min in Fig. 2a. As shown in Fig. 2a, the concentration of toluene remained constant without catalyst under UV–Vis irradiation, indicating that the bright light couldn't remove toluene without catalyst. The pure TiO_2 samples synthesized by wet precipitation or sol–gel methods exhibited poor activities for toluene degradation. The removal efficiency was ~ 20% in 10 min and then declined rapidly, which may be related to the accumulation of intermediates [36]. With the introduction of CuO, the removal efficiency of toluene was dramatically increased. The removal efficiency of the composites prepared by wet precipitation method was higher (almost 10%) than that prepared by sol–gel method. Conversely, the TiO_2(S) exhibited better performance than TiO_2(P), which was probably attributed to the darker color of TiO_2(S) sample with stronger light absorption. 2Cu2Ti(P) exhibited the best activity as demonstrated by its highest toluene removal efficiency of 80% within 120 min. Furthermore, the long-term stability of photocatalytic performance was shown in Fig. 2b. The removal efficiency of toluene could remain at around 80% and the CO_2 yield was almost 90% at least 480 min owing to the synergetic effect between photocatalysis and thermal catalysis. The results also revealed that the catalyst had a superior stability and better mineralization. As shown in Fig. 2c, the efficiency on 2Cu2Ti(P) decreased slightly after four cycles, meaning its excellent durability for toluene oxidation.

The effects of operating conditions were discussed in Fig. 2d using 2Cu2Ti(P), including the initial concentration of toluene, the air flow rate, the illumination intensity and the coexistence of water. On the whole, the higher initial concentration of toluene can inhibit the catalytic process on account of the limited active sites and competitive adsorption [37,38]. The removal efficiency of toluene decreased as the air flow rate increased. At a high flow rate, the toluene had a shorter residence time with catalysts indicating an incomplete catalytic oxidation [39,40]. As shown in Fig. 2d, the removal efficiency of toluene dropped greatly with the illumination intensity of Xe lamp decreasing. The higher illumination intensity promoted the formation of electron-hole pairs, leading to more reactive oxygen species. Importantly, there was lower photon flux under the lower illumination intensity resulting in fewer electrons getting excited [41]. As we can see in Fig. 2d, the water molecule had weak impact on catalytic process with a faint trend of first increasing and then decreasing. On the one hand, H_2O is not only a catalytic product of toluene, but also a reactant for the formation of reactive oxygen species [38]. On the other hand, the competitive adsorption of H_2O became weaker with the increase of temperature driven by light [42].

3.2. Morphology and structure

The morphology of 2Cu2Ti composites prepared by different methods was characterized by the SEM and TEM. 2Cu2Ti(P) was a cluster structure, composed of stacked particles with the particle size of about 100–160 nm (Fig. 3a-b). Further observation revealed the lattice spacing (0.369 nm) and interplanar spacing (0.372 nm) in the TEM image of 2Cu2Ti(P), which attributed to TiO_2 (1 0 1) plane. It also found the lattice spacing (0.231 nm) and interplanar spacing (0.213 nm) corresponding to CuO (1 1 1) plane in Fig. 3c. While the sample prepared by sol–gel method was a layered structure. As we can see in Fig. 3d-e, the layered structure of 2Cu2Ti(S) was composed of 30–50 nm particles. The lattice spacing of about 0.327 nm and interplanar spacing of about 0.336 nm can be observed in Fig. 3f, which was assigned to TiO_2 (1 0 1) plane. There were different interplanar spacings of CuO (0.232 and 0.262 nm) attributing to (1 1 1) plane and (11–1) plane, respectively. And the lattice spacings of those planes were 0.241 and 0.269 nm. Those results indicated that larger particle size might be more favorable for removal toluene. The EDX images of 2Cu2Ti(P) are showed in Fig. 3g-i,

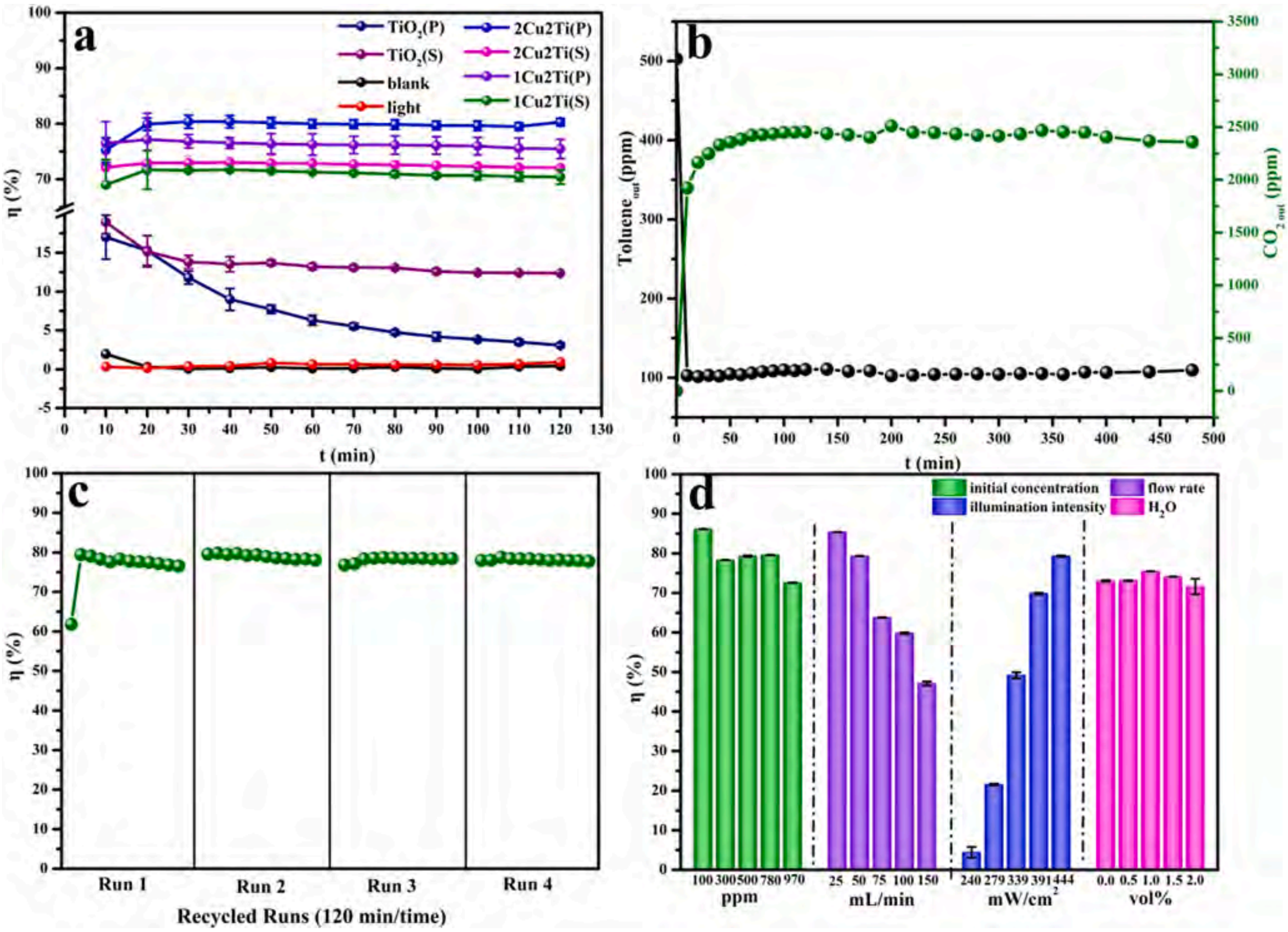

Fig. 2. (a) Catalytic activities of samples in degradation of toluene under UV–Vis light irradiation. (500 ppm toluene; air flow rate, 50 mL/min; illumination intensity, 444 mW/cm^2, 0 vol% H_2O) (b) The stability of 2Cu2Ti(P) for removal toluene under UV–Vis irradiation. (c) The recycled runs of 2Cu2Ti(P) composite for removal toluene under UV–Vis irradiation. (d) The removal efficiencies of toluene under different operating conditions at 120 min.

and it is clear that Ti and Cu species were homogeneously dispersed on the surface of catalyst. As shown in Table 1, the weight percentage of Cu was 48.30%, and the weight percentage of Ti was 25.94%, which results were slightly different from that of XPS. The atomic percentages of Cu and Ti were obtained by EDX and XPS, and the calculated Cu/Ti ratio was higher than theoretical value referring to the molar ratio of Cu and Ti in the precursors during the preparation process, which implied that CuO was more likely to grow on the surface.

Fig. 4 shows the N_2 adsorption–desorption isotherms and pore size distribution of the samples prepared by the different methods. It can be seen that except for TiO_2(S), the N_2 adsorption–desorption isotherms of other catalysts exhibited type Ⅳ isotherms. Meanwhile, 1Cu2Ti(S), TiO_2(P), 1Cu2Ti(P), and 2Cu2Ti(P) showed H2 type hysteresis loop, which indicated that the pore structures of the catalysts exhibited dense stacked spherical particle interstitial pores, while 2Cu2Ti(S) showed H3 type hysteresis loop and the catalyst had a lamellar slit structure [43]. During the preparation process with sol–gel method, the structure of catalyst was gradually loosened with the introduction of CuO, and finally 2Cu2Ti(S) exhibited a lamellar structure, which was consistent with the results of SEM. The adsorption–desorption isotherm of TiO_2(S) was straight line approximately revealing that TiO_2(S) had a small specific surface area (5.10 m^2/g) and poor pore structure. As shown in the Table 2, the specific surface areas of five catalysts with type Ⅳ isotherms were relatively close, and 2Cu2Ti(P) had the largest specific surface area. The pore size distribution diagram showed that the pore sizes of the catalysts were in the range of 4–8 nm and all of them had mesoporous structures [44].

The phase and crystallite structure of obtained samples are described in Fig. 5a. These peaks located at 25.28°, 37.80°, 48.05°, 53.89°, 55.06°, 62.69°, 68.76°, 70.31°, 75.21° were assigned to (1 0 1), (0 0 4), (2 0 0), (1 0 5), (2 1 1), (2 0 4), (1 1 6), (2 2 0), (2 1 5) planes of anatase TiO_2 (JCPDS PDF#21–1272). The diffraction peaks at 32.51°, 35.54°, 38.71°, 48.72°, 61.52° were the characteristic peaks of monoclinic CuO (JCPDS PDF#48–1548), which could be indexed to (1 1 0), (11–1), (1 1 1), (20–2), (11–3) planes, respectively. Those results were consistent with the results from TEM. The sharp shapes and high intensity of those diffraction peaks revealed high crystallinity of those samples [43]. With the introduction of CuO, some diffraction peaks of TiO_2 disappeared and the diffraction peak at 25.28° was significantly weakened. The crystallite sizes of catalysts were listed in Table 2, which were calculated according to the Debye-Scherrer equation [45]. The results indicated the smaller particle of CuO/TiO_2 and the existence of interactions between TiO_2 and CuO, which facilitated electron transfer [46]. It is worth noting that the peak intensity of the composites prepared by wet precipitation method was higher than the composites prepared by sol–gel method, which indicated that 2Cu2Ti(P) had a larger particle size and higher crystallinity.

The surface composition and chemical states of the samples were studied by XPS. The related XPS spectra of O 1s, Ti 2p, and Cu 2p of the obtained catalysts are shown in Fig. 5b-d. For O 1s pattern, the obvious peak at about 529.90 eV was attributed to surface lattice oxygen (O_L), and the peak at about 531.62 eV corresponded to surface adsorbed oxygen species (O_A), respectively [47,48]. The peaks of O_L slightly shifted toward lower binding energy revealing the electron cloud density of O

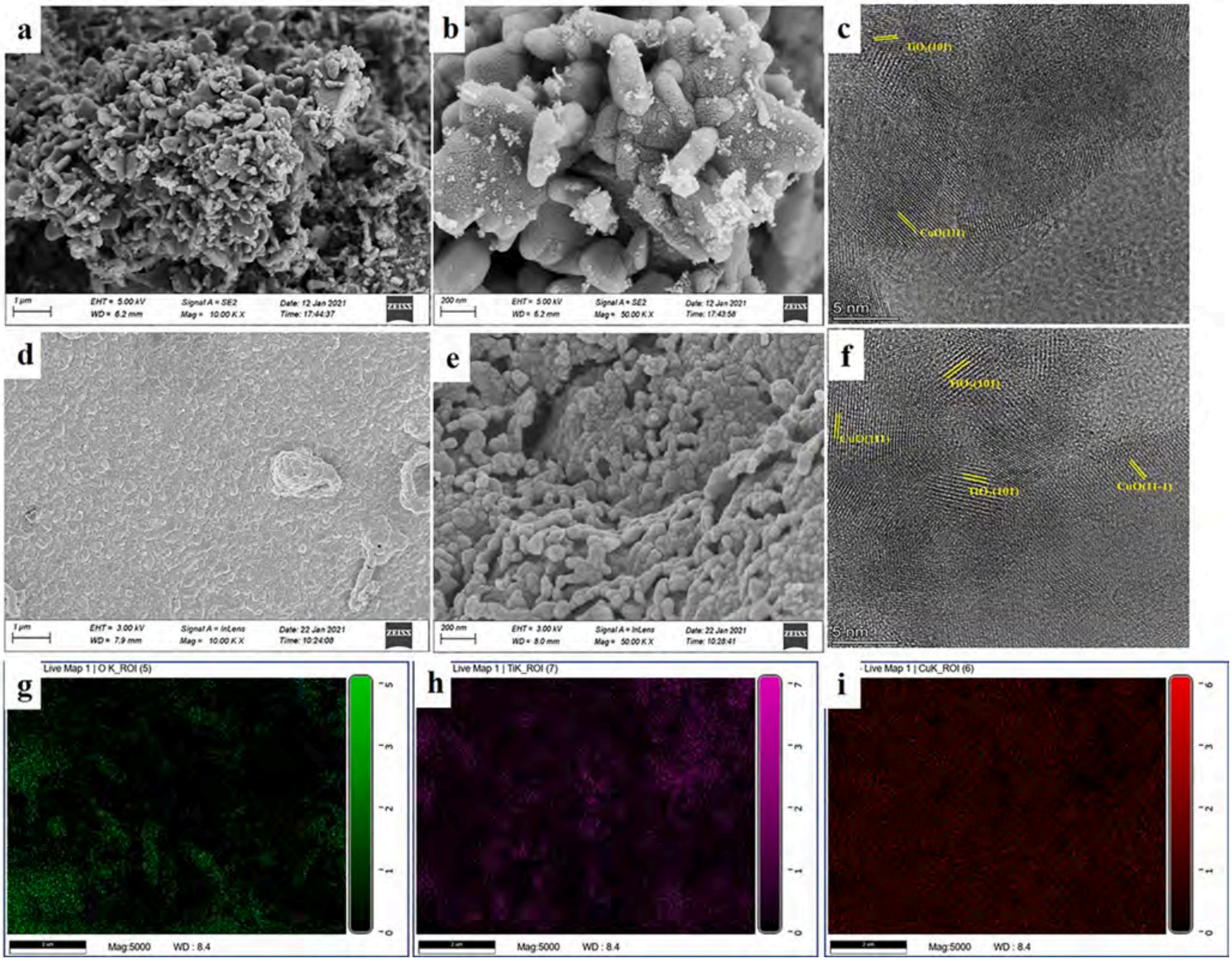

Fig. 3. The electron microscopy images of 2Cu2Ti composites prepared by different methods. (a-b) SEM of 2Cu2Ti(P), (c) TEM of 2Cu2Ti(P), (d-e) SEM of 2Cu2Ti(S), (f) TEM of 2Cu2Ti(S), and EDX mapping images of (g) O, (h) Ti, and (i) Cu elements of 2Cu2Ti(P).

Table 1
The atoms of 2Cu2Ti(P) sample calculated by EDX data and XPS data.

Atom	EDX			XPS	
	Atomic (%)	Weight (%)	Error (%)	Atomic (%)	Weight (%)
O	53.98	25.76	8.06	61.77	31.30
Ti	17.68	25.94	2.46	16.65	25.25
Cu	28.34	48.30	3.11	21.58	43.45

species increased and the activity of O_L increased [49,50]. It was reported that O_A can be seen from Table 3 that with the increase of CuO the amount of O_A rose, which can trap photogenerated electrons to generate reactive oxygen species, thus improving the photocatalytic activity [51]. Moreover, there was a peak at 533.53 eV of 2Cu2Ti(S) corresponding to H-O-H of crystal water (O_H), which might be the result of solvent ethanol [16]. In the case of Ti 2p, the peaks at about 458.64 eV and 464.30 eV were ascribed to Ti $2p_{1/2}$ and Ti $2p_{3/2}$ of Ti^{4+} in anatase TiO_2, respectively [9,52]. It was found that the Ti 2p peaks moved toward low binding energy obviously with the introduction of CuO, which was probably attributed to the interfacial interactions between TiO_2 and CuO [20]. For the Cu 2p deconvolution, six peaks implied two kinds of Cu species. The peaks at about 934.41 eV and 954.33 eV were ascribed to Cu^{2+}, while the peaks at about 932.50 eV and 952.54 eV were attributed to Cu^{+} [30,53]. In addition, there were two peaks at about 941.11 eV and 943.73 eV assigned to the satellite peak [32,35]. The Cu^{+}/Cu^{2+} ratios in CuO/TiO_2 composites rapidly increased with the increase of CuO. The existence of Cu^{+} might be beneficial to the adsorption and activation of oxygen, thus enhancing the catalytic performance [31,54]. The Cu^{+}/Cu^{2+} ratio of 2Cu2Ti(P) was highest contributing to the best catalytic performance of 2Cu2Ti(P). As we can be seen from Table 3, the Cu/Ti ratio in 2Cu2Ti(S) was much higher than the theoretical value referring to the molar ratio of Cu and Ti in the precursors during the preparation process, which implied that the dispersion of CuO prepared by wet precipitation method was better than that of the sol–gel method.

3.3. *Photoelectrical property*

The UV–Vis absorption spectra of the pure TiO_2 and composites were compared and shown in Fig. 6a. The pure TiO_2 samples had stronger absorption capacity in the ultraviolet range (about 300–380 nm) and then dropped conspicuously in the visible region (about 380–800 nm). Furthermore, the TiO_2(S) with a color of gray had stronger optical absorption than the TiO_2(P) with a color of white in the visible region. Surprisingly, the absorption of obtained composites was strong in visible region. On the one hand, CuO could strengthen the response of TiO_2 to the visible region clearly attributing to CuO with a narrow bandgap. On the other hand, the composites could be seen as dark materials with excellent light absorption capacity [17]. Especially, 2Cu2Ti(P) exhibited

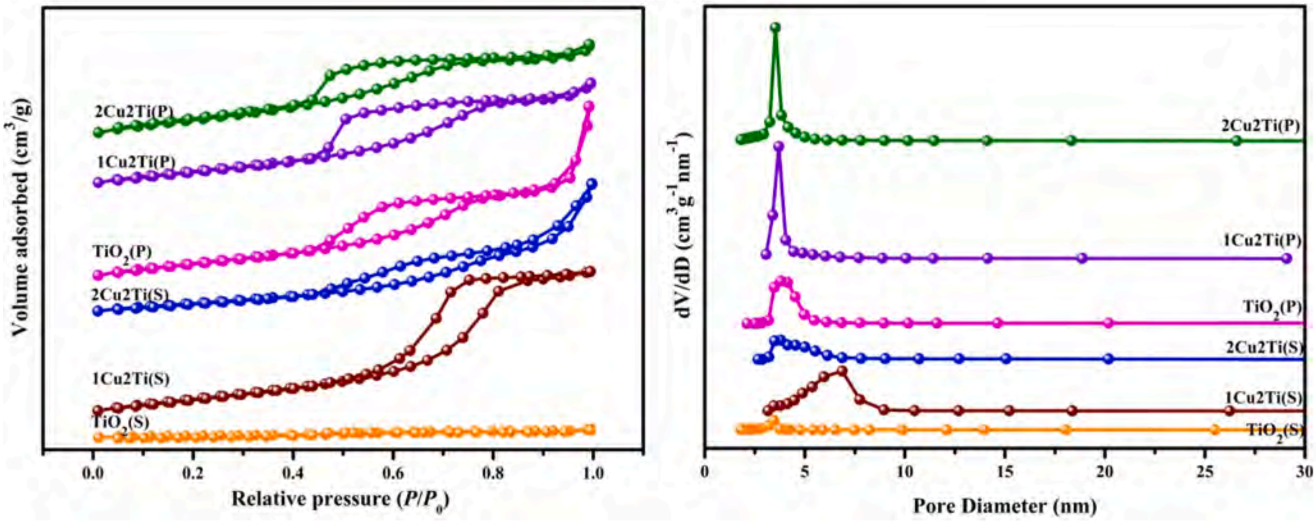

Fig. 4. N_2 adsorption–desorption isotherms and the pore size distribution of catalysts.

Table 2
The textural properties of samples.

Samples	Crystal size ^{a}(nm)	Crystal size ^{b}(nm)	BET surface area(m^2/g)	Pore volume (cm^3/g)	Average pore diameter (nm)
TiO_2(S)	11	0	5.10	0.01	4.06
1Cu2Ti (S)	10	31	50.07	0.10	6.15
2Cu2Ti (S)	10	43	32.08	0.07	7.08
TiO_2(P)	25	0	46.91	0.07	7.64
1Cu2Ti (P)	8	91	45.96	0.07	4.19
2Cu2Ti (P)	4	greater than300	51.97	0.06	4.12

Crystal size ^{a}: The crystal size of TiO_2
Crystal size ^{b}: The crystal size of CuO

the largest absorption capacity of light. The transient photocurrent is commonly used to represent the recombination rate of charges, which is an important factor in the process of photocatalysis. The transient photocurrent of composites was measured under Xe lamp irradiation (Fig. 6b). With the content of CuO increasing, the response of transient photocurrent increased and the recombination rate of charges declined due to the formation of an internal electric field [55]. The 2Cu2Ti(P) exhibited the highest response of transient photocurrent, revealing that 2Cu2Ti(P) had a stronger separation of electron-hole pairs. The inhibition of recombination for photogenerated electron-hole pairs could increase the active radicals, thereby enhancing the degradation of toluene [37].

It has been reported that the active radicals ($\cdot$OH, $\cdot O_2^-$) play important parts in the photocatalytic degradation of toluene [11,56,57]. The reactive oxygen species generated by 2Cu2Ti(P) sample were characterized by EPR spectra with DMPO (Fig. 6c, d). There were feeble signals and no significant signal change of $\cdot$OH between dark and Xe lamp irradiation, revealing that water molecular could not be oxidized to $\cdot$OH on the 2Cu2Ti(P) both in dark and under illumination. In other words, the valence band (VB) edge potential of 2Cu2Ti(P) might be negative than the standard redox potential of $\cdot OH/H_2O$ pair [58]. Therefore, the water weakly promoted this catalytic process. In Fig. 6d, no signal of $\cdot O_2^-$ was detected in dark. On the contrary, there was a clear signal on 2Cu2Ti (P) under Xe lamp irradiation. It was suggested that $\cdot O_2^-$ radical could be formed by redox of O_2 with the photogenerated charges.

3.4. The photocatalysis and thermalcatalysis

To further investigate the contributions of photocatalysis and thermalcatalysis, the degradation of toluene was studied under different conditions with 2Cu2Ti(P) composite. 2Cu2Ti(P) exhibited lower activity (~60%), lower CO_2 yield (60%) and lower durability with an ice bath in Fig. 7a, revealing that the heat driven by UV–Vis irradiation accelerated and sustained the process of toluene removal. The removal efficiency of toluene under the full spectrum was also studied to match the sun light. The temperature of the reactor increased to 180 ℃ with the introduction of infrared (IR) and the efficiency increased to 90%. As shown in Fig. 7, the temporal temperature varied with UV–Vis and UV–Vis-IR irradiation in reactor was measured and the efficiency at each temperature was badly lower (18% and 39%), implying that the effect of thermo-catalysis was smaller than photocatalysis for light-driven photothermal catalytic degradation. With the introduction of heat driven by light, the CO_2 yield increased from 60% to 90% in Fig. 7a, which revealed that heat could promote the mineralization process and desorption of CO_2. Therefore, the heat generated by irradiation might accelerate the reaction kinetics depending on the Arrhenius formula and reduce the deposition of intermediates, thus releasing more active sites and improving the performance [59–61]. It can be inferred from the results that the photocatalysis had dominating effect in the process, in which the migration of electrons was occurred under irradiation to generate reactive oxygen species, thus participating in toluene degradation.

To further investigate the process of toluene removal, the used 2Cu2Ti(P) obtained under different reaction conditions were characterized, respectively. The surface functional groups of fresh and used 2Cu2Ti(P) were shown in Fig. 8a. The absorption band below 850 cm^{-1} was assigned to the stretching vibrations of Cu-O and Ti-O [58]. The peaks at 2800–2900 cm^{-1} were attributed to the C-H stretching vibration of adsorbed toluene, and the broad bands at 1400–1600 cm^{-1} were corresponding to the C=O and O-C-O vibrations of intermediates [61,62]. The peaks of 2Cu2Ti(P)-P were stronger than that of 2Cu2Ti(P)-T and 2Cu2Ti(P)-PT. The results revealed that heat driven by light reduced the accumulation of intermediates and increased the exposure of active sites, thereby improving catalytic activity and durability. The atoms (O, Ti, and Cu) on the surface of sample 2Cu2Ti(P) were measured in detail (Fig. 8b-d). There were new peaks beyond 532.00 eV about O 1s attributing to O-H in the used catalyst, which probably owed to the adsorption of product H_2O. As listed in Table 3, the O_A/O_L of the used catalyst was slightly higher than the fresh catalyst. It may be because gaseous O_2 were preferentially adsorbed on the oxygen vacancies under

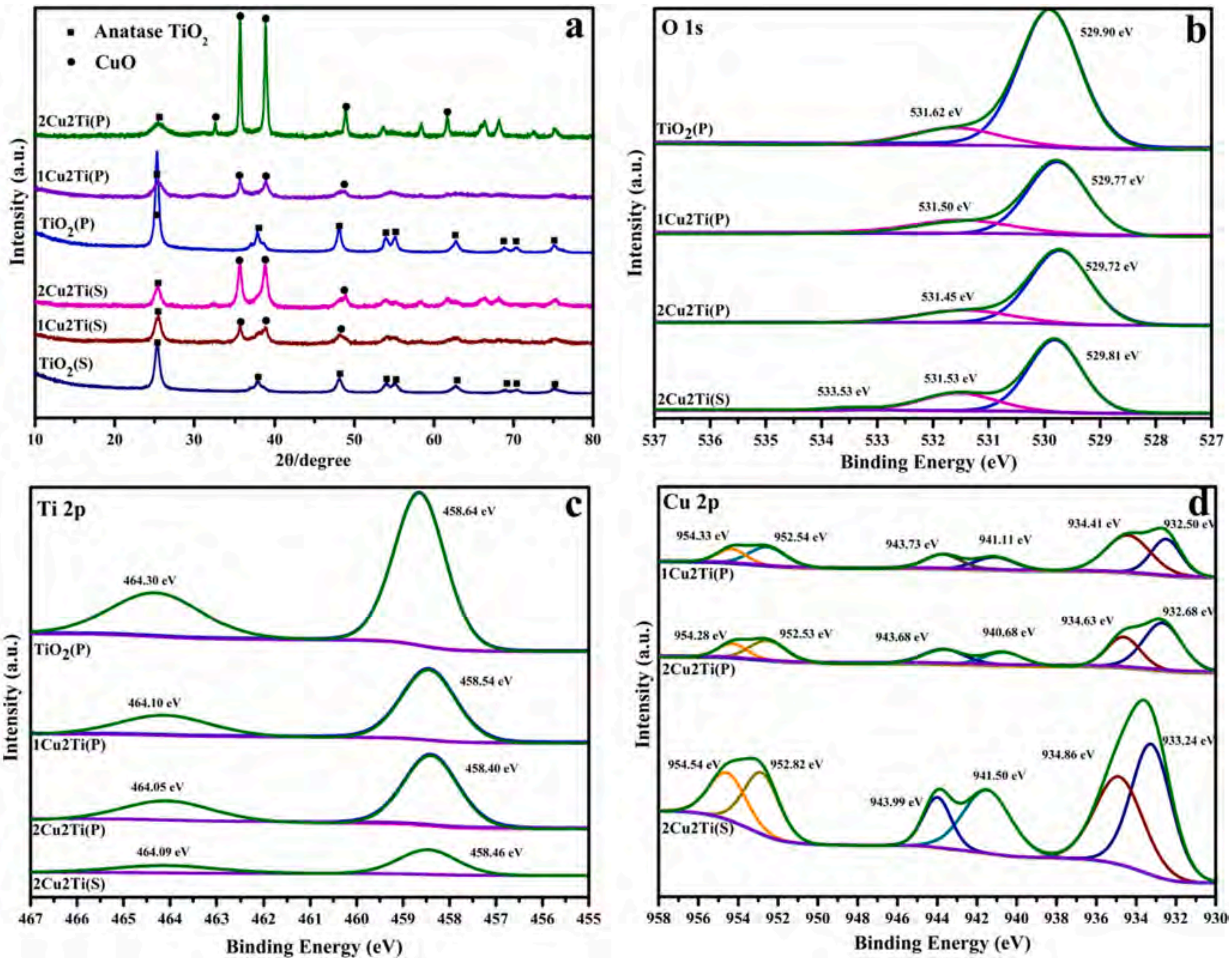

Fig. 5. (a) XRD patterns of obtained samples. XPS spectra of fresh catalysts, (b) O 1 s, (c) Ti 2p, (d) Cu 2p.

Table 3
The surface element composition of samples.

samples	O_A/O_L	O_H/O	Cu/Ti	Cu^+/Cu^{2+}
TiO_2(P)	0.16	–	–	–
1Cu2Ti(P)	0.26	–	0.29	0.88
2Cu2Ti(P)	0.27	–	1.29	1.81
2Cu2Ti(S)	0.35	0.02	2.80	1.24
2Cu2Ti(P)-PT [a]	0.29	0.04	2.46	1.62
2Cu2Ti(P)-T [b]	0.28	0.03	2.03	1.22
2Cu2Ti(P)-P [c]	0.27	0.04	2.72	1.18

[a] the used 2Cu2Ti(P) sample obtained catalytic reaction under UV–Vis irradiation (120 min).

[b] the used 2Cu2Ti(P) sample obtained thermo-catalysis at 240 ℃ for 120 min.

[c] the used 2Cu2Ti(P) sample obtained catalysis under UV–Vis irradiation with ice-bath (120 min).

an oxygen-rich atmosphere, which may promote the complete oxidation of toluene and facilitate better stability of the catalyst [11,30]. It also could be noted that a new peak (460.60 eV) appeared in the used catalyst, which ascribed to the generation of Ti^{3+} in the photocatalytic process [63]. As shown in Fig. 8d, the binding energy of Cu 2p increased after reaction, revealing that the electron cloud density of Cu species reduced. It was also found that the ratio of Cu^+/Cu^{2+} decreased after reactions.

3.5. The reaction path and mechanism

The removal mechanism of toluene was revealed through in situ DRIFTs spectra obtained under UV–Vis irradiation on the surface of catalyst. As shown in Fig. 9, it can be observed that the absorption peak at 1635 cm^{-1} was associated with the framework vibration of the aromatic ring. And the bands at 3045 and 3084 cm^{-1} could be attributed to the vibration about C-H of aromatic hydrogen, which revealed the presence of the adsorbed toluene [54,61]. Besides, the peaks at 2877 and 2940 cm^{-1} assigned asymmetric and symmetric C-H stretching vibrations of methyl group were also observed [17]. The peaks of adsorbed toluene increased under dark and then gradually reduced with UV–Vis irradiation, meaning that toluene was accumulated on the surface of catalyst under dark and effectively removed with UV–Vis irradiation. It happens that there was a strong peak at 3440 cm^{-1} detected on the catalyst surface, which was attributed to the hydroxyl group. The increased peak was probably caused by the generation of H_2O. Some slight peaks from 1000 cm^{-1} to 1200 cm^{-1} were corresponding to benzyl alcohol [49]. The benzaldehyde species were detected at weak peaks about 1412, 1431, and 1453 cm^{-1} [54]. The absorption bands at 1505 and 1364 cm^{-1} could be observed apparently attributing to –COO stretch modes of benzoate species [61,64]. There were small amounts of benzyl alcohol, benzaldehyde, and benzoic acid on the catalyst surface under dark, attributing to a certain degree of oxidation [54]. As the time of illumination went, the peak intensity of benzoic acid significantly increased, implying that more benzoic acid was accumulated on the

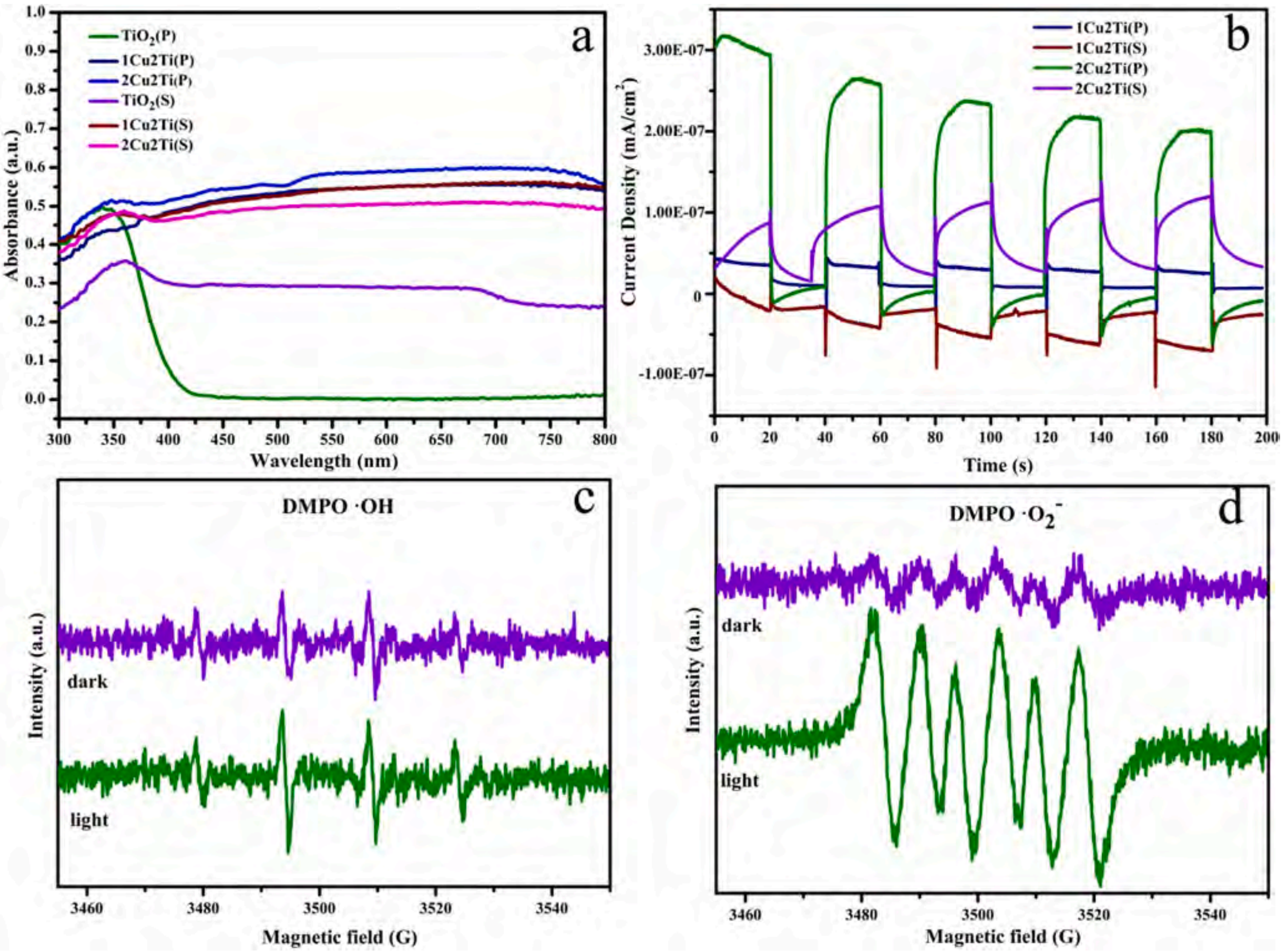

Fig. 6. (a) UV–Vis diffuse reflectance spectra of the obtained catalysts. (b) Transient photocurrent response curves of the prepared composites. Reactive oxygen species (c) ·OH and (d) $\cdot O_2^-$ of 2Cu2Ti(P) sample with DMPO at room temperature. The signals were collected under dark and Xe lamp irradiation, respectively.

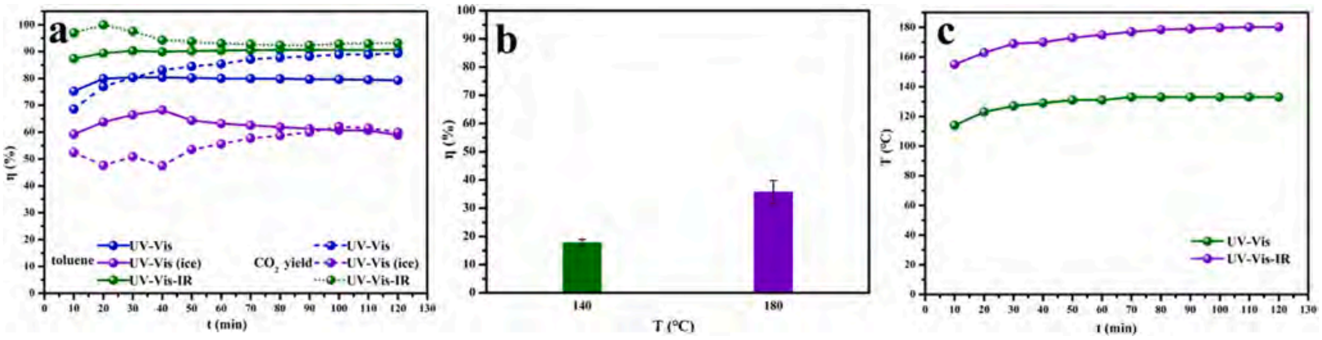

Fig. 7. (a) Catalytic activity of 2Cu2Ti(P) for removal toluene with Xe lamp irradiation. (b) Thermal catalytic activity of 2Cu2Ti(P) for removal toluene. (c) Temporal temperature evolution with the irradiation in reactor. (500 ppm toluene; air flowrate, 50 mL/min; illumination intensity, 444 mW/cm^2, 0 vol% H_2O).

catalyst surface. This may be due to high ring-opening reaction energy for benzoic acid [62]. Notably, it was found the attenuate peaks of the benzene ring because the benzene ring was opened under UV–Vis irradiation. A new peak at 1313 cm^{-1} gradually appeared identified with maleic acid and maleic anhydride, and peaks at 1715 and 1735 cm^{-1} were corresponded to chain fatty acid, which are important intermediates in the ring-opening process of aromatic compounds [11,50,65]. Furthermore, the final product CO_2 at peak 2332 cm^{-1} was discovered [61].

In order to deeply investigate the photothermal catalysis, the band gap energy of TiO_2 and CuO was calculated using Tauc plots and Mott-Schottky plots in Fig. S1. According to the above results, 2Cu2Ti(P) could be excited to generate e^-/h^+ pairs under Xe lamp irradiation (Fig. 10). The conduction band (CB) of TiO_2 was more negative than that of CuO. Therefore, the photo-generated electrons were transferred from the CB of CuO to the CB of TiO_2, which promoted the separation of charges and increased the lifetime of electrons. The photoexcited electrons gathered in the CB of TiO_2 as active sites, which could be captured by the adsorbed O_2 to produce $\cdot O_2^-$ specie. The h^+ in the VB of TiO_2 moved to the VB of CuO. Meanwhile, the photo-generated h^+ might take

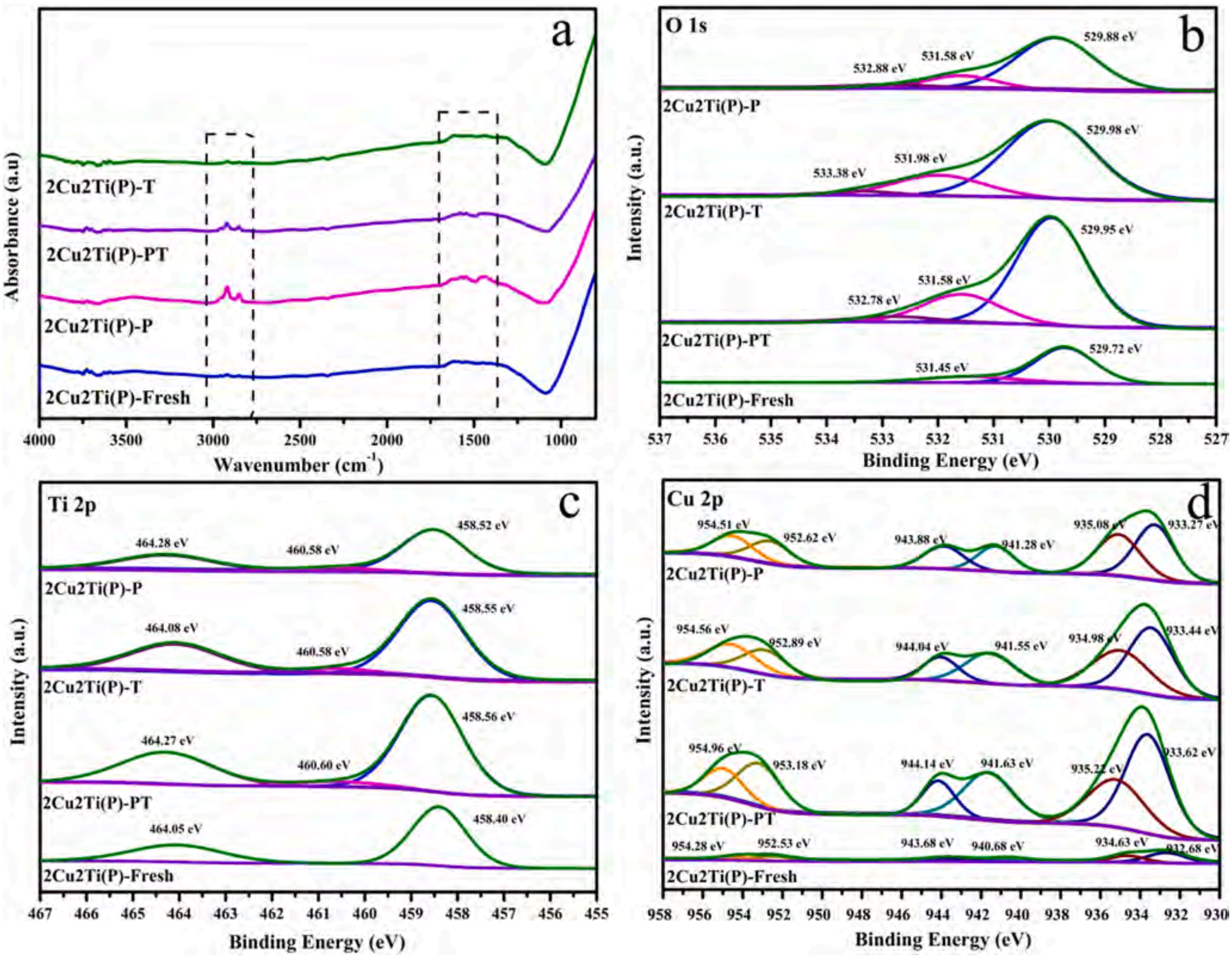

Fig. 8. (a) FTIR spectra of fresh and used 2Cu2Ti(P), (b) XPS of O 1 s, (c) XPS of Ti 2p, and (d) XPS of Cu 2p about 2Cu2Ti(P) sample before and after reactions.

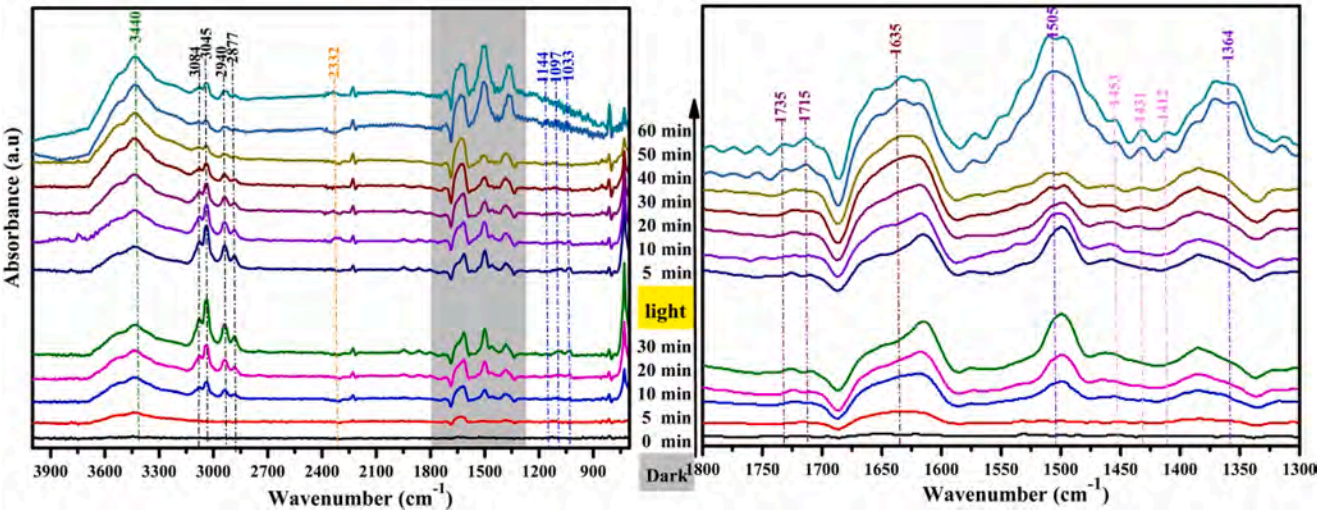

Fig. 9. (a) In situ DRIFTS spectra of toluene removal over 2Cu2Ti(P) composite under dark and Xe lamp irradiation. (b) partial magnification spectra at the wavenumber range of 1800–1300 cm^{-1}.

part in the photocatalytic process directly because ·OH radical couldn't be formed on the surface. Under attack with $\cdot O_2^-$ and h^+, the adsorbed toluene was rapidly oxidized to benzyl alcohol, benzaldehyde, and benzoic acid. Then, the aromatic ring was opened to form maleic acid. In the end, the chain fatty acids and anhydrides were mineralized into CO_2 and H_2O.

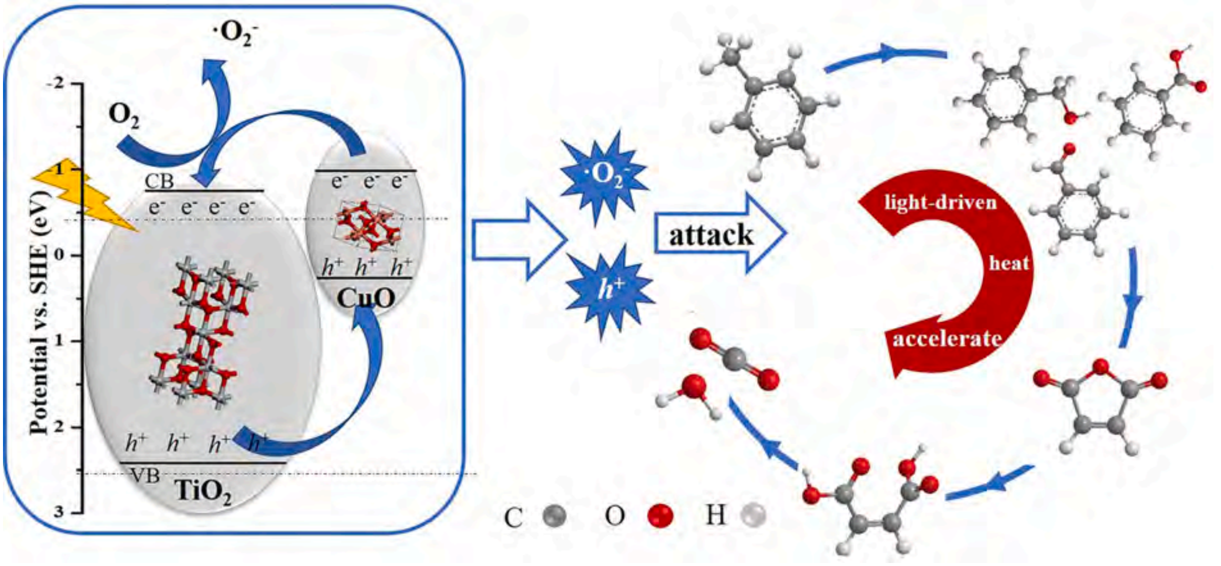

Fig. 10. The proposed mechanism for the degradation of toluene.

4. Conclusion

This work provides a promising strategy using light-driven photothermal catalysis over the composites of CuO/TiO_2 to enhance light absorption, which improves its photothermal catalytic performance for toluene removal. Compared with samples prepared by sol–gel method, 2Cu2Ti(P) has a larger particle size and narrower band gap. The 2Cu2Ti (P) exhibited excellent performance and stability for toluene degradation, attributing to the stronger separation of charges and absorption of light. The synergistic effect of light and heat promoted the removal of toluene obviously, and the photocatalysis played a major role. In this process, toluene was attacked by $\cdot O_2^-$ and h^+ to produce intermediates such as benzoic acid, eventually mineralizing to CO_2 and H_2O. What's more, the intensity of light and air flow greatly affected the removal efficiency of toluene in the photothermal catalytic process. The CuO/TiO_2 composites are expected to have potential application in photothermal catalysis to make full use of solar energy.

CRediT authorship contribution statement

Caixia Liang: Methodology, Validation, Formal analysis, Writing – original draft. **Caiting Li:** Conceptualization, Resources, Writing – review & editing, Funding acquisition. **Youcai Zhu:** Conceptualization, Validation, Writing – review & editing. **Xueyu Du:** Investigation, Writing – review & editing. **Yifu Zeng:** Resources, Funding acquisition. **Yihui Zhou:** Resources, Funding acquisition. **Jungang Zhao:** Data curation, Writing – review & editing. **Shanhong Li:** Supervision, Project administration. **Xuan Liu:** Writing – review & editing, Project administration. **Qi Yu:** Software, Visualization. **Yunbo Zhai:** Supervision, Project administration.

Declaration of Competing Interest

The authors declare that they have no known competing financial interests or personal relationships that could have appeared to influence the work reported in this paper.

Acknowledgements

This work was supported by the Key Research and Development Program of Hunan Province in China (2018SK2032, 2018SK2033), and the National Key Research and Development Program of China (2016YFC0204100).

Appendix A. Supplementary material

Supplementary data to this article can be found online at https://doi.org/10.1016/j.apsusc.2022.154144.

References

[1] Y. Liu, M. Song, X. Liu, Y. Zhang, L. Hui, L. Kong, Y. Zhang, C. Zhang, Y. Qu, J. An, Characterization and sources of volatile organic compounds (VOCs) and their related changes during ozone pollution days in 2016 in Beijing, China, Environmental Pollution 257 (2020), 113599.
[2] K.T. Malecha, S.A. Nizkorodov, Photodegradation of secondary organic aerosol particles as a source of small, oxygenated volatile organic compounds, Environ. Sci. Technol. 50 (2016) 9990–9997.
[3] T. An, Y. Huang, G. Li, Z. He, J. Chen, C. Zhang, Pollution profiles and health risk assessment of VOCs emitted during e-waste dismantling processes associated with different dismantling methods, Environ. Int. 73 (2014) 186–194.
[4] S. Nayek, P.K. Padhy, Personal exposure to VOCs (BTX) and women health risk assessment in rural kitchen from solid biofuel burning during cooking in West Bengal, India, Chemosphere 244 (2020), 125447.
[5] W.S. Choi, M.J. Hwang, Y. Kwon, S. Jung, Y. Youn, M.S. Balathanigaimani, J. Lee, K. Hwang, W. Shim, Radio-frequency thermal plasma treated activated carbon impregnated with Mn and Ag for volatile organic compounds adsorption, Journal of Nanoscience, Nanotechnology 20 (2020) 4423–4427.
[6] Y. Lyu, C. Li, X. Du, Y. Zhu, Y. Zhang, S. Li, Catalytic oxidation of toluene over MnO_2 catalysts with different Mn (II) precursors and the study of reaction pathway, Fuel 262 (2020), 116610.
[7] B. Song, C. Li, X. Du, S. Li, Y. Zhang, Y. Lyu, Q. Zhou, Superior performance of Cu-Ce binary oxides for toluene catalytic oxidation: Cu-Ce synergistic effect and reaction pathways, Fuel 306 (2021), 121654.
[8] Y. Zhang, M. Wu, Y. Wang, Y.H. Kwok, W. Pan, W. Szeto, H. Huang, D.Y.C. Leung, Fluorinated TiO_2 coupling with α-MnO_2 nanowires supported on different substrates for photocatalytic VOCs abatement under vacuum ultraviolet irradiation, Appl. Catal. B 280 (2021), 119388.
[9] J. Qu, D. Chen, N. Li, Q. Xu, H. Li, J. He, J. Lu, Ternary photocatalyst of atomic-scale Pt coupled with MoS_2 co-loaded on TiO_2 surface for highly efficient degradation of gaseous toluene, Appl. Catal. B 256 (2019), 117877.
[10] H. Ren, P. Koshy, W. Chen, S. Qi, C.C. Sorrell, Photocatalytic materials and technologies for air purification, J. Hazard. Mater. 325 (2017) 340–366.
[11] L. Chen, P. Chen, H. Wang, W. Cui, J. Sheng, J. Li, Y. Zhang, Y. Zhou, F. Dong, Surface lattice oxygen activation on $Sr_2Sb_2O_7$ enhances the photocatalytic mineralization of toluene: from reactant activation, intermediate conversion to product desorption, ACS Appl. Mater. Interfaces 13 (2021) 5153–5164.
[12] E. Yu, J. Li, J. Chen, J. Chen, Z. Hong, H. Jia, Enhanced photothermal catalytic degradation of toluene by loading Pt nanoparticles on manganese oxide: Photoactivation of lattice oxygen, J. Hazard. Mater. 388 (2020), 121800.
[13] X. Xie, Y. Li, Y. Yang, C. Chen, Q. Zhang, UV-Vis-IR driven thermocatalytic activity of OMS-2/SnO_2 nanocomposite significantly enhanced by novel photoactivation and synergetic photocatalysis-thermocatalysis, Appl. Surf. Sci. 462 (2018) 590–597.

[14] Z. Shi, L. Lan, Y. Li, Y. Yang, Q. Zhang, J. Wu, G. Zhang, X. Zhao, Co_3O_4/TiO_2 nanocomposite formation leads to improvement in ultraviolet-visible-infrared-driven thermocatalytic activity due to photoactivation and photocatalysis-thermocatalysis synergetic effect, ACS Sustainable Chemistry Engineering 6 (2018) 16503–16514.

[15] Y. Tang, Y. Tao, T. Zhou, B. Yang, Q. Wang, Z. Zhu, A. Xie, S. Luo, C. Yao, X. Li, Direct Z-scheme $La_{1\text{-}x}Ce_xMnO_3$ catalyst for photothermal degradation of toluene, Environ. Sci. Pollut. Res. 26 (2019) 36832–36844.

[16] P. Wu, S. Dai, G. Chen, S. Zhao, Z. Xu, M. Fu, P. Chen, Q. Chen, X. Jin, Y. Qiu, S. Yang, D. Ye, Interfacial effects in hierarchically porous $\alpha\text{-}MnO_2/Mn_3O_4$ heterostructures promote photocatalytic oxidation activity, Appl. Catal. B 268 (2020), 118418.

[17] J. Li, E. Yu, S. Cai, X. Chen, J. Chen, H. Jia, Y. Xu, Noble metal free, $CeO_2/LaMnO_3$ hybrid achieving efficient photo-thermal catalytic decomposition of volatile organic compounds under IR light, Appl. Catal. B 240 (2019) 141–152.

[18] E. Yu, J. Chen, H. Jia, Enhanced light-driven photothermocatalytic activity on selectively dissolved $LaTi_{1\text{-}x}Mn_xO_{3+\delta}$ perovskites by photoactivation, J. Hazard. Mater. 399 (2020), 122942.

[19] Z. Shayegan, C.S. Lee, F. Haghighat, TiO_2 photocatalyst for removal of volatile organic compounds in gas phase - a review, Chem. Eng. J. 334 (2018) 2408–2439.

[20] T. Xu, H. Zheng, P. Zhang, Isolated Pt single atomic sites anchored on nanoporous TiO_2 film for highly efficient photocatalytic degradation of low concentration toluene, J. Hazard. Mater. 388 (2020), 121746.

[21] Z. Rao, G. Shi, Z. Wang, A. Mahmood, X. Xie, J. Sun, Photocatalytic degradation of gaseous VOCs over $Tm^{3+}\text{-}TiO_2$: revealing the activity enhancement mechanism and different reaction paths, Chem. Eng. J. 395 (2020), 125078.

[22] R. Xie, D. Lei, Y. Zhan, B. Liu, C.H.A. Tsang, Y. Zeng, K. Li, D.Y.C. Leung, H. Huang, Efficient photocatalytic oxidation of gaseous toluene over F-doped TiO_2 in a wet scrubbing process, Chem. Eng. J. 386 (2020), 121025.

[23] M. Li, W. Song, L. Zeng, D. Zeng, C. Xie, Q. Yang, Mechanistic study of N-H- and H-N-codoping of a TiO_2 photocatalyst for efficient degradation of benzene under visible light, RSC Adv. 10 (2020) 2757–2766.

[24] Y. Zhang, M. Wu, Y.H. Kwok, Y. Wang, W. Zhao, X. Zhao, H. Huang, D.Y.C. Leung, In-situ synthesis of heterojunction TiO_2/MnO_2 nanostructure with excellent performance in vacuum ultraviolet photocatalytic oxidation of toluene, Appl. Catal. B 259 (2019), 118034.

[25] A. Akhundi, A. Badiei, G.M. Ziarani, A. Habibi-Yangjeh, M.J. Muñoz-Batista, R. Luque, Graphitic carbon nitride-based photocatalysts: Toward efficient organic transformation for value-added chemicals production, Molecular Catalysis 488 (2020), 110902.

[26] S. Asadzadeh-Khaneghah, A. Habibi-Yangjeh, $g\text{-}C_3N_4$/carbon dot-based nanocomposites serve as efficacious photocatalysts for environmental purification and energy generation: A review, J. Cleaner Prod. 276 (2020), 124319.

[27] Y. Xin, Q. Chen, G. Zhang, Construction of ternary heterojunction $CuS\text{-}CdS/TiO_2$ nanobelts for photocatalytic degradation of gaseous toluene, J. Alloy. Compd. 751 (2018) 231–240.

[28] W. Wang, Y. Zhang, J. Zhang, G. Li, D. Leng, Y. Gao, J. Gao, H. Lu, X. Li, Metal-organic framework-derived $Cu_2O\text{-}CuO$ octahedrons for sensitive and selective detection of ppb-level NO_2 at room temperature, Sens. Actuators, B 328 (2021), 129045.

[29] R. Gusain, P. Kumar, O.P. Sharma, S.L. Jain, O.P. Khatri, Reduced graphene oxide-CuO nanocomposites for photocatalytic conversion of CO_2 into methanol under visible light irradiation, Appl. Catal. B 181 (2016) 352–362.

[30] Y. Wang, D. Yang, S. Li, L. Zhang, G. Zheng, L. Guo, Layered copper manganese oxide for the efficient catalytic CO and VOCs oxidation, Chem. Eng. J. 357 (2019) 258–268.

[31] Y. Zhang, C. Li, Y. Zhu, X. Du, Y. Lyu, S. Li, Y. Zhai, Insight into the enhanced performance of toluene removal from simulated flue gas over Mn-Cu oxides modified activated coke, Fuel 276 (2020), 118099.

[32] L. Yang, J. Guo, T. Yang, C. Guo, S. Zhang, S. Luo, W. Dai, B. Li, X. Luo, Y. Li, Self-assembly Cu_2O nanowire arrays on Cu mesh: a solid-state, highly-efficient, and stable photocatalyst for toluene degradation under sunlight, J. Hazard. Mater. 402 (2021), 123741.

[33] S. Zhang, X. Gong, Q. Shi, G. Ping, H. Xu, A. Waleed, G. Li, CuO nanoparticle-decorated TiO_2-nanotube heterojunctions for direct synthesis of methyl formate via photo-oxidation of methanol, ACS Omega 5 (2020) 15942–15948.

[34] M. Chen, H. Wang, X. Chen, F. Wang, X. Qin, C. Zhang, H. He, High-performance of $Cu\text{-}TiO_2$ for photocatalytic oxidation of formaldehyde under visible light and the mechanism study, Chem. Eng. J. 390 (2020), 124481.

[35] W. Zhou, B. Shen, F. Wang, X. Zhang, Z. Zhao, M. Si, S. Guo, Enhanced photocatalytic degradation of xylene by blackening TiO_2 nanoparticles with high dispersion of CuO, J. Hazard. Mater. 391 (2020), 121642.

[36] W. Zhang, G. Li, H. Liu, J. Chen, S. Ma, M. Wen, J. Kong, T. An, Photocatalytic degradation mechanism of gaseous styrene over Au/TiO_2@CNTs: relevance of superficial state with deactivation mechanism, Appl. Catal. B 272 (2020), 118969.

[37] J. Duan, X. Song, H. Zhao, Z. Zhang, W. Wang, Self-assembled flower-like $(BiO)_2CO_3\text{-}CdS\text{-}CuS$ stable heterojunction degrades toluene under visible light response, Opt. Mater. 101 (2020), 109761.

[38] S. Saqlain, B.J. Cha, S.Y. Kim, T.K. Ahn, C. Park, J.-M. Oh, E.C. Jeong, H.O. Seo, Y. D. Kim, Visible light-responsive Fe-loaded TiO_2 photocatalysts for total oxidation of acetaldehyde: fundamental studies towards large-scale production and applications, Appl. Surf. Sci. 505 (2020), 144160.

[39] A. Mahmood, G. Shi, X. Xie, J. Sun, Assessing the adsorption and photocatalytic activity of TiO_2 nanoparticles for the gas phase acetaldehyde: A computational and experimental study, J. Alloy. Compd. 819 (2020), 153055.

[40] W. Zhou, Z. Guan, M. Zhao, J. Li, Characteristics and mechanism of toluene removal from gas by novelty array double dielectric barrier discharge combined with TiO_2/Al_2O_3 catalyst, Chemosphere 226 (2019) 766–773.

[41] A. Jonoidi Jafari, M. Kermani, A. Hosseini-Bandegharaei, A. Rastegar, M. Gholami, A. Alahabadi, G. Farzi, Synthesis and characterization of Ag/TiO_2/composite aerogel for enhanced adsorption and photo-catalytic degradation of toluene from the gas phase, Chem. Eng. Res. Des. 150 (2019) 1–13.

[42] Z. Lin, X. Tong, W. Shen, J.C. Roux, H. Xi, Humidity impact on photo-catalytic degradation: adsorption behavior simulations and catalytic reaction mechanisms for main gaseous pollutants in papermaking industry, J. Cleaner Prod. 244 (2020), 118863.

[43] J. Chen, X. Chen, X. Chen, W. Xu, Z. Xu, H. Jia, J. Chen, Homogeneous introduction of CeO_y into MnO_x-based catalyst for oxidation of aromatic VOCs, Appl. Catal. B 224 (2018) 825–835.

[44] L. Zhao, Z. Zhang, Y. Li, X. Leng, T. Zhang, F. Yuan, X. Niu, Y. Zhu, Synthesis of $CeaMnO_x$ hollow microsphere with hierarchical structure and its excellent catalytic performance for toluene combustion, Appl. Catal. B 245 (2019) 502–512.

[45] Z. Sihaib, F. Puleo, J.M. Garcia-Vargas, L. Retailleau, C. Descorme, L.F. Liotta, J. L. Valverde, S. Gil, A. Giroir-Fendler, Manganese oxide-based catalysts for toluene oxidation, Appl. Catal. B 209 (2017) 689–700.

[46] Y. Shu, Y. Xu, H. Huang, J. Ji, S. Liang, M. Wu, D.Y.C. Leung, Catalytic oxidation of VOCs over Mn/TiO_2/activated carbon under 185nm VUV irradiation, Chemosphere 208 (2018) 550–558.

[47] J. Kong, Z. Xiang, G. Li, T. An, Introduce oxygen vacancies into CeO_2 catalyst for enhanced coke resistance during photothermocatalytic oxidation of typical VOCs, Appl. Catal. B 269 (2020), 118755.

[48] X. Yang, S. Liu, J. Li, J. Chen, Z. Rui, Promotion effect of strong metal-support interaction to thermocatalytic, photocatalytic, and photothermocatalytic oxidation of toluene on $Pt/SrTiO_3$, Chemosphere 249 (2020), 126096.

[49] W. Yang, Z. Su, Z. Xu, W. Yang, Y. Peng, J. Li, Comparative study of α-, β-, γ- and $\delta\text{-}MnO_2$ on toluene oxidation: Oxygen vacancies and reaction intermediates, Environmental, Applied Catalysis B, 2019, p. 118150.

[50] Y. Shen, J. Deng, S. Impeng, S. Li, T. Yan, J. Zhang, L. Shi, D. Zhang, Boosting toluene combustion by engineering Co-O strength in cobalt oxide catalysts, Environ. Sci. Technol. 54 (2020) 10342–10350.

[51] G. He, J. Zhang, Y. Hu, Z. Bai, C. Wei, Dual-template synthesis of mesoporous TiO_2 nanotubes with structure-enhanced functional photocatalytic performance, Appl. Catal. B 250 (2019) 301–312.

[52] L. Mohan V, S.M. Shiva Nagendra, M.P. Maiya, Photocatalytic degradation of gaseous toluene using self-assembled air filter based on chitosan/activated carbon/TiO_2, Journal of Environmental Chemical Engineering, 7 (2019) 103454-103455.

[53] P. Wei, D. Qin, J. Chen, Y. Li, M. Wen, Y. Ji, G. Li, T. An, Photocatalytic ozonation mechanism of gaseous n-hexane on $MO_x\text{-}TiO_2$-foam nickel composite (M = Cu, Mn, Ag): unveiling the role of ·OH and $\cdot O_2^-$, Environmental Science, NANO 6 (2019) 959–969.

[54] J. Li, K. Li, B. Lei, M. Ran, Y. Sun, Y. Zhang, K.H. Kim, F. Dong, High-efficiency photocatalytic decomposition of toluene over defective InOOH promotive role of oxygen vacancies in ring opening process, Chem. Eng. J. 413 (2021), 127389.

[55] Y. Liu, C. Zhu, J. Sun, Y. Ge, F. Song, Q. Xu, In situ assembly of $CQDs/Bi_2WO_6$ for highly efficient photocatalytic degradation of VOCs under visible light, New J. Chem. 44 (2020) 3455–3462.

[56] Q. Chen, L. Liu, L. Liu, Y. Zhang, A novel UV-assisted PEC-MFC system with CeO_2/TiO_2/ACF catalytic cathode for gas phase VOCs treatment, Chemosphere 126930 (2020).

[57] A. Habibi-Yangjeh, S. Asadzadeh-Khaneghah, S. Feizpoor, A. Rouhi, Review on heterogeneous photocatalytic disinfection of waterborne, airborne, and foodborne viruses: Can we win against pathogenic viruses? J. Colloid Interface Sci. 580 (2020) 503–514.

[58] J. Liu, P. Wang, W. Qu, H. Li, L. Shi, D. Zhang, Nanodiamond-decorated ZnO catalysts with enhanced photocorrosion-resistance for photocatalytic degradation of gaseous toluene, Appl. Catal. B 257 (2019), 117880.

[59] A.J. Jafari, R.R. Kalantary, A. Esrafili, H. Arfaeinia, Synthesis of silica-functionalized graphene oxide/ZnO coated on fiberglass and its application in photocatalytic removal of gaseous benzene, Process Saf. Environ. Prot. 116 (2018) 377–387.

[60] A.J. Jafari, R.R. Kalantari, M. Kermani, M.H. Firooz, ZnO nanoparticles photocatalytic activity toward atmospheric toluene under simulated sunlight, Res. Chem. Intermed. 46 (2019) 119–131.

[61] Z. Chen, Y. Peng, J. Chen, C. Wang, H. Yin, H. Wang, C. You, J. Li, Performance and mechanism of photocatalytic toluene degradation and catalyst regeneration by thermal/UV treatment, Environ. Sci. Technol. 54 (2020) 14465–14473.

[62] P. Chen, W. Cui, H. Wang, X. Dong, J. Li, Y. Sun, Y. Zhou, Y. Zhang, F. Dong, The importance of intermediates ring-opening in preventing photocatalyst deactivation during toluene decomposition, Appl. Catal. B 272 (2020), 118977.

[63] T.-D. Pham, B.-K. Lee, C.-H. Lee, The advanced removal of benzene from aerosols by photocatalytic oxidation and adsorption of $Cu\text{-}TiO_2$/PU under visible light irradiation, Appl. Catal. B 182 (2016) 172–183.

[64] J. Li, G. Zhang, W. Cui, W. Cen, Z. Wu, S.C. Lee, F. Dong, Probing ring-opening pathways for efficient photocatalytic toluene decomposition, J. Mater. Chem. A 7 (7) (2019) 3366–3374.

[65] P. Sun, W. Wang, X. Dai, X. Weng, Z. Wu, Mechanism study on catalytic oxidation of chlorobenzene over $Mn_xCe_{1\text{-}x}O_2$/H-ZSM5 catalysts under dry and humid conditions, Appl. Catal. B 198 (2016) 389–397.